Ultrasensitive Visual Tracking of Toxic Cyanide Ions in Biological Samples Using Biocompatible Metal–organic Frameworks Architectures

I.M. El-Sewify [a,b], M.A. Shenashen[a,c], R.F. ElAgamy[d], M.S. Selim[c], N.F. Alqahtani[e], A. Elmarakbi [f], M. Ebara[a], M.M. Selim[g], M.M.H. Khalil[b], S.A. El-Safty[a,].*

[a] Research Center for Macromolecules and Biomaterials, National Institute for Materials Science (NIMS), 1-2-1 Sengen, Tsukubashi, Ibaraki-ken 305-0047, Japan

[b] Department of Chemistry, Faculty of Science, Ain Shams University, 11566 Cairo, Abbassia, Egypt

[c] Department of Petrochemical, Egyptian Petroleum Research Institute (EPRI), Nasr City, 11727 Cairo, Egypt

[d] College of Computer Science and Engineering, Taibah University, Yanbu, 966144 Saudi Arabia

[e] Department of Chemistry, College of Science, University of Jeddah, Jeddah 21589, Saudi Arabia

[f] Faculty of Engineering and Environment, Northumbria University, Newcastle Upon Tyne, NE1 8ST, UK.

[g] Al-Aflaj College of Science and Human Studies, Prince Sattam Bin Abdulaziz University, Al-Aflaj 710-11912, Saudi Arabia

E-mail: sherif.elsafty@nims.go.jp; & sherif.el-safty@sunderland.ac.uk

Homepage: https://samurai.nims.go.jp/profiles/sherif_elsafty

ABSTRACT

The extraordinary accumulation of cyanide ions within biological cells is a severe health risk. Detecting and tracking toxic cyanide ions within these cells by simple and ultrasensitive methodologies are of immense curiosity. Here, continuous tracking of ultimate levels of CN^{-}-ions in HeLa cells was reported employing biocompatible branching molecular architectures (BMAs). These BMAs were engineered by decorating colorant-laden dendritic branch within and around the molecular building hollows of the geode-shelled nanorods of organic–inorganic Al-frameworks. Batch-contact methods were utilized to assess the potential of hollow-nest architecture for inhibition/evaluation of toxicant CN^{-}-ions within HeLa cells. The nanorod BMAs revealed significant potential capabilities in monitoring and tracking of CN− ions (88 parts per trillion) in biological trials within seconds. These results demonstrated sufficient evidence for the compatibility of BMAs during HeLa cell exposure. Under specific conditions, the BMAs were utilized for in-vitro fluorescence tracking/sensing of CN^{-} in HeLa cells. The cliff swallow nest with massive mouths may have the potential to reduce the health hazards associated with toxicant exposure in biological cells.

KEYWORDS: Visual Monitoring; Cyanide; HeLa cells; In-vitro; Biocompatible; Al-MOF Nanorods.

Environmental Implication:

Aquatic ecosystems and human health are seriously threatened by cyanide. This study describes the creation of biocompatible materials for monitoring/tracking CN^{-}-ions in water and biological samples.

1. INTRODUCTION

The manipulation of cyanide in global industry is foreseeable. Raw materials containing cyanide are significantly utilized in dyes, electroplating, and fibers [1]. The toxic cyanide can be promptly combined with hemoglobin and promote organism death via preventing oxygen transfer in the human body, and minimal cyanide doses is enormously poisonous [2,3]. The World Health Organization proposes the threshold safety for cyanide concentration (1.9 μM) in drinking water [3,4]. In this regard, the recognition of CN^- has attracted worldwide scientific concern.

Many methodologies, such as potentiometric, voltammetry, and electrochemical have been studied to determine CN^- ions [5-7]. Novel technologies have been utilized for detecting ultra-trace concentrations of cyanide ions [8-16]. The creation of chemosensors by confining sensitive and selective probes into porous structures has earned widespread acclaim in the field of tracking and detecting many targets [17-21]. Chemical and physical decorations are the two foremost procedures in designing chemosensors [22- 27]. The trapping of colorant receptors by using physical process is uncomplicated. However, critical alignments of colorant receptors over the porous platform are expected due to the organic receptor discharge in tested solution. In addition, the drawbacks of the designed chemosensors using chemical methods are instability and one-time use [28-39]. The decoration procedures of chromophores onto nanoporous platform are an extremely effective technique for creating sensors with long-term stability [40].

The common weakness of grafting process is the unorganized binding events of organic probes into the porous carrier surface, and this drawback may restrict the carrier's active site. Numerous analytical techniques were applied in biological cells to track and enumerate ultra-trace toxic pollutants and monitor common pollutants. The conventional approaches [41- 43] can

significantly identify the concentration and distribution of toxic species in living samples [44]. However, these classical approaches associated with intensive handling and training and expensive operating procedures may lead to dull detection of toxic pollutants.

Inorganic–organic frameworks have recently received research attention due to the high porosity and crystallinity of metal–organic frameworks (MOFs) [45]. They are composed of metal ions and organic linkers to design uniform structures. The linker structure arrangement enhances the surface area and controls the construction of organic–inorganic frameworks [46-49]. The optical chemosensors using MOFs as carrier improved the sensing potential compared with the reported chemosensors for various purposes, such as catalysis, adsorption, and carriers for luminescence [50-53]. Moreover, the inorganic–organic framework platforms, which are stacked with chromophores, have been applied for monitoring toxicants in different applications [54].

In this study, the fabricated biocompatible branching molecular architectures (BMAs) revealed prospective functions in cyanide tracking in HeLa cells within seconds. The BMA stability and structural morphology were examined. The organic aggregates crust layer within and around the inorganic–organic framework cavities approved for fabricating BMAs geodes and offered continuous tracking of CN^- ions in HeLa cells. The findings demonstrated evidence for monitoring/tracking CN^- ions in HeLa cells by using BMA hierarchal geodes (Scheme 1) and for the high biocompatibility of the designed optical chemosensors during exposure and monitoring of CN^- ions in HeLa cells. This study offers a novel method for utilizing metal–organic frameworks in biological and environmental evaluations.

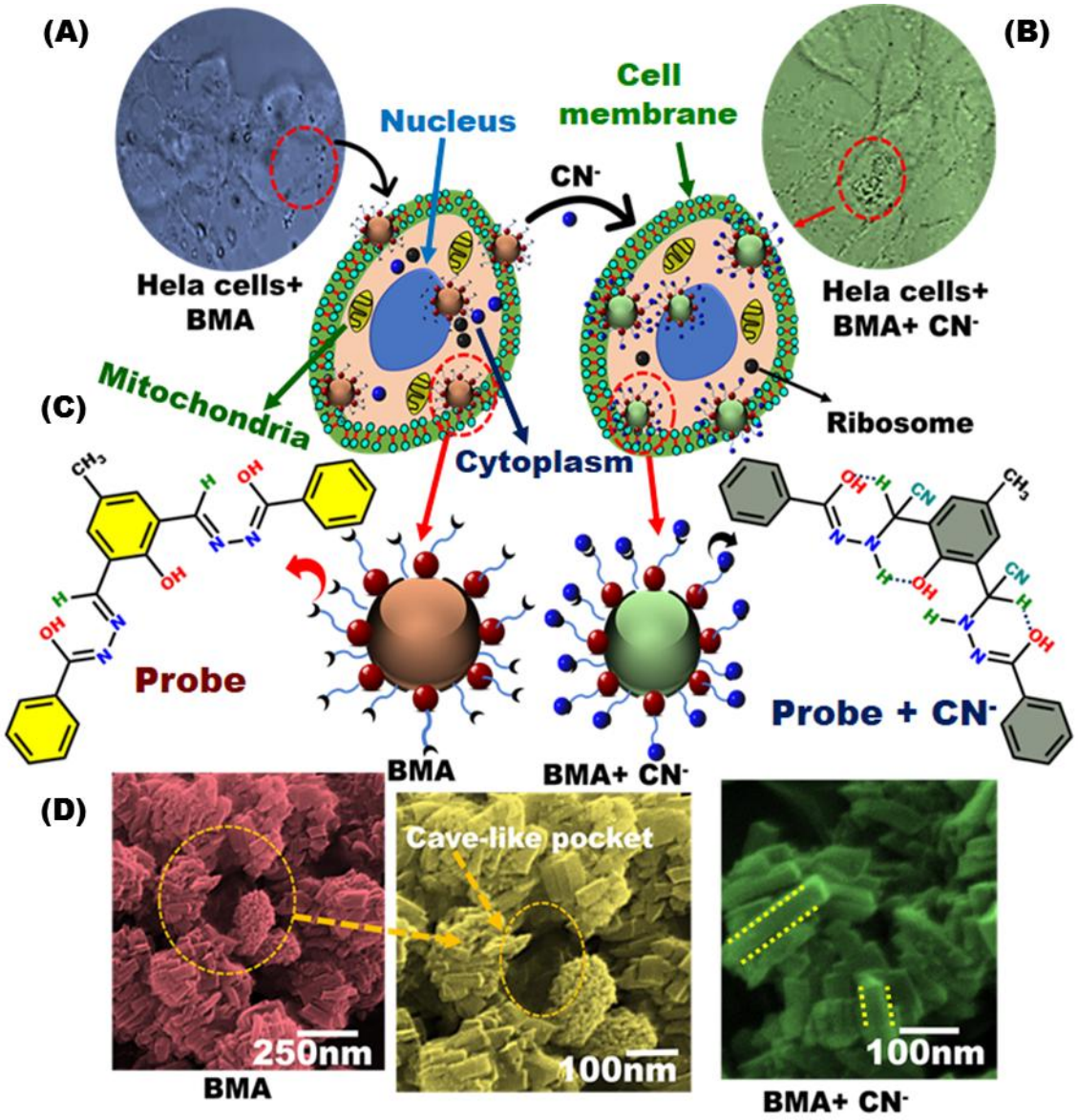

Scheme 1. Schematic representation of tracking and capturing of CN^- ions in living cell via using BMA geodes. The bright field images of the contaminated HeLa cell (A) and the treated HeLa show high fluorescence enhancement after formation of the complex [BMA-CN^-](B). After incubation of HeLa cells for 24 hours, a 20 µg /ml of [BMA] 100 ppb of CN^- ions were added and incubated for 24 hours. The BMA geodes were fabricated via immobilization of organic receptors into the microporous surface of BMA geodes (C). The FE-SEM images (D) show the high morphological stability of nanorods with geodes shells crystals of BMA.

2. EXPERIMENTAL SECTION

2.1. Chemicals and Materials

For preparation of organic chromophore, 2-hydroxy-5-methylisophthalaldehyde, Benzohydrazide were purchased from Wako chemicals, Tokyo, Japan. To fabricate inorganic -organic frameworks, Aluminum nitrate nonahydrate ($Al(NO_3)_3 \cdot 9H_2O$), the organic linker 2-terephthalic acid in mixed solvent N,N-dimethylformamide chemicals were obtained from Sigma-Aldrich. To adjust the pH of the solution, (HEPES) buffer and disodium hydrogen phosphate were used. All used solvents were analytical reagents and ethanol was used for spectral recognition. To perform the selectivity toward cyanide (CN^-), we evaluated using common interfering anions including F^-, Br^-, Cl^-, I^-, NO_3^-, CH_3COO^-, $H_2PO_4^-$, SO_4^{2-}, ClO_4^-, HSO_4^-.

2.2. Fabrication of BMA

A one-pot solvothermal approach was applied using a mixed solvent containing N,N-dimethylformamide (DMF) and water to fabricate supermicroporous Al-MOF nanorods. 1,4-Benzenedicarboxylic acid (0.56 g) and $Al(NO_3)_3.9H_2O$ (0.51 g) were mixed with the solvent. After the mixture was stirred for 5 mins, it was heated in an autoclave at 160 °C overnight. The white powder obtained was purified using the mixed solvent. The engineered Al-MOF nanorods were stimulated by boiling with methanol overnight at 80 °C to remove unreacted and trapped organic linkers within the Al-MOF micropores. Direct decoration was performed to design optical chemosensors. The Al-MOF nanorods (0.5 g) were stirred with organic chromophore ethanolic solution (0.1 g) until saturation. The removal of solvent resulted in the discoloration of the Al-MOF nanorods, indicating the stacking of the prepared organic receptor L1 into the supermicroporous cavities. The decoration process was repeated several times, and the nanorods

were dried to 60 °C for 12 h to verify the loading of supermicroporous cavities in the Al-MOF nanorods.

2.3. Cytotoxicity Studies

The cell feasibility of the receptors and BMA were examined on HeLa cell lines by using methylthiazolyldiphenyl-tetrazolium bromide (MTT) assay. The cells were seeded into a well plate at 50×10^4 cells per well and incubated in a medium containing the receptor and BMA at concentrations ranging from 0 μg/ml to 50 μg/ml for 24 h. MTT (100 μL) was added to each well and incubated by reacting with metabolically active HeLa cells. The MTT and media were discarded from the well plate. Dimethyl sulfoxide was added to each well to suspend intracellular formazan crystals, and the microplates were shaken for 10 mins. A microplate reader was used to record the change in absorbance intensity.

3. RESULTS AND DISCUSSION

3.1 Fabrication of Decorated Nanorod Architectures

One-pot, simple, and template-free assays were conducted to examine the construction of geode-shelled inorganic–organic frameworks. The engineering of BMA geodes was successfully created using the direct decoration process of dendritic branch aggregates into super-microporous scaffold for tracking and monitoring of CN^- ions in biological samples. The results revealed uniform nanorod branches along swirled caves with multifunctional surfaces. The fabricated BMAs were designed via physical immobilization, and the organic linker showed a significant characteristic in designing uniform construction with high-surface-area carriers under solvothermal condition [55- 63]. The direct immobilization process resulted in homogenous BMAs with outer and interior nanorod surface. Moreover, the binding between the receptors and the active centers in the carrier surface at room temperature is achieved by van der Waals and

hydrogen bonding interactions (Scheme 2). The swirled caves along the branches and organic nature of the Al-MOF carriers augmented the physical interactions between the multifunction surface of nanorods and the j-aggregate probes. Moreover, the binding affinity of BMA chemosensors with CN^- ions was enhanced, and fast recognition was observed under optimal requirements.

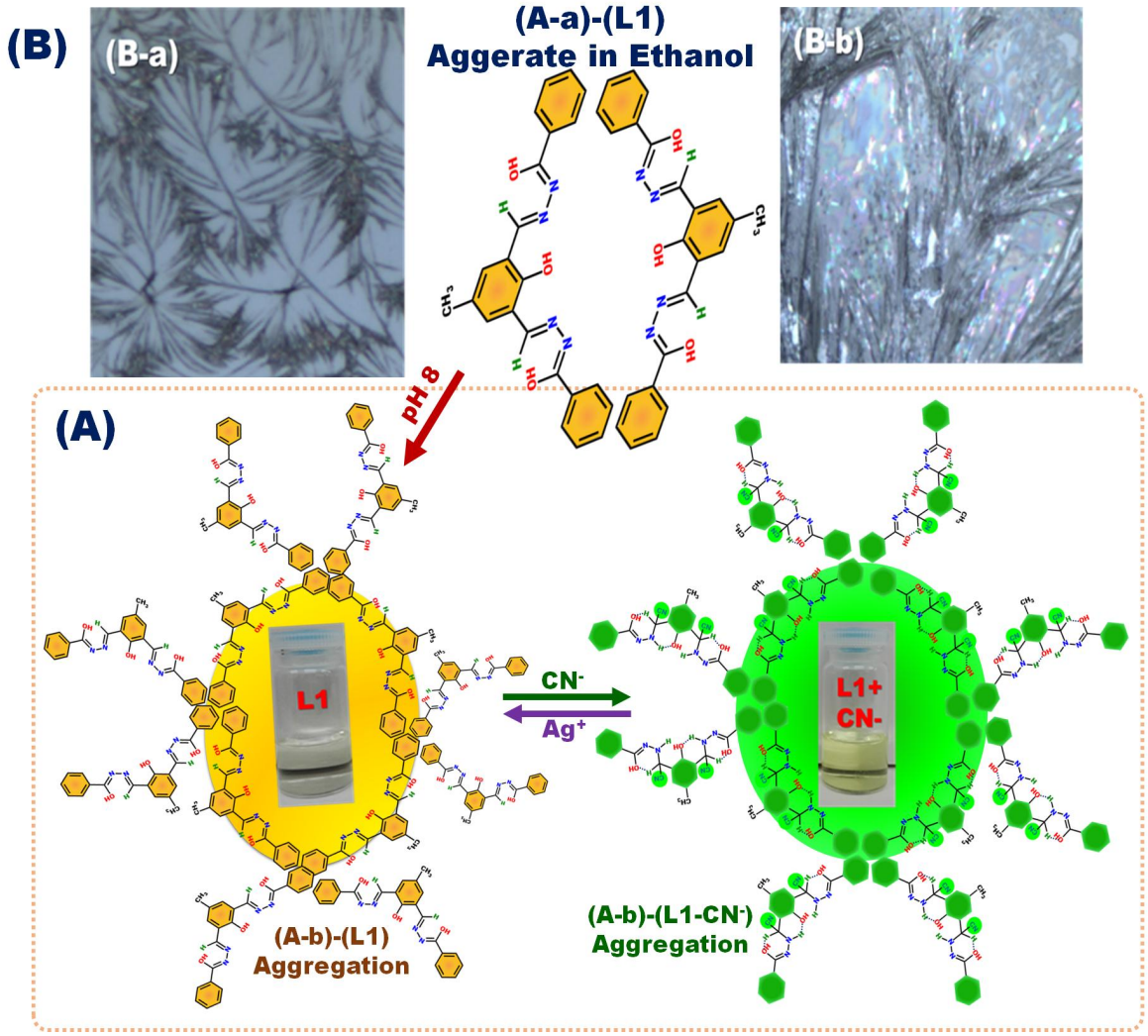

Scheme 2. (A & B) Structural formation and optical images of the colorant and fluorescent J-aggregates of L1 receptor and its [L1-CN] complex with dendritic spine stacking arrangement of parallel alignment of L1 colorant fiber in ethanol (B-a) and dendritic branches (B-b) molecular

151 directional structure of L1 colorant at pH 8 and during the formation of [L1-CN] complex with
152 addition of CN^- ions, respectively.

153 **3.2. Structure Characterization**

154 Field-emission scanning electron microscopy (FESEM) were conducted to investigate the
155 development of nest-shaped carriers, which were combined and distributed as hierarchal geodes
156 (Figures 1A and 1B). The results showed that the 50–100 nm Al-MOF geode-shelled nanorod
157 structures were ordered of asymmetrical open-pore systems that linked across the entire and with
158 the cage cavities. As shown in Figure 1, the data showed the formation of a chaotically shaped
159 window, well-arranged nanorods, and a cliff swallow nest with massive mouths. The FESEM
160 images revealed advancement of supermicroporous cavities to confine the organic probes and
161 hallow interior structure (Figures 1C–1E). The polyrods of Al-MOFs uniformly accumulated and
162 aggerated around the massive mouths.

163 The well-organized Al-MOF stability with hierarchal geode shells was explained using the
164 atomic force microscopic images in Figure 1G. The TEM images confirmed the formation of
165 external crust layers via simple immobilization of dendritic branch around the BMAs. The
166 components of BMA hierarchical engineering were as follows:

167 (i) Randomly shaped channels and active facet {101} of inorganic–organic-Al
168 framework cliff swallow nest with massive mouths structures enabled trapping of
169 receptors.

170 (ii) Uniform virtual and dense sheath colorant constructions were formed.

171 (iii) The aggerates inside the microchannels allowed for the hierarchical engineering of
172 BMA geodes.

(iv) The crust layer of organic chromophores showed simultaneous tracking, fast response time, and binding of toxic CN^- compounds.

(v) Retention of BAMs' multifunctional binding sites during electron or charge transport led to an extensive range of cyanide colorant tracking in biological cells.

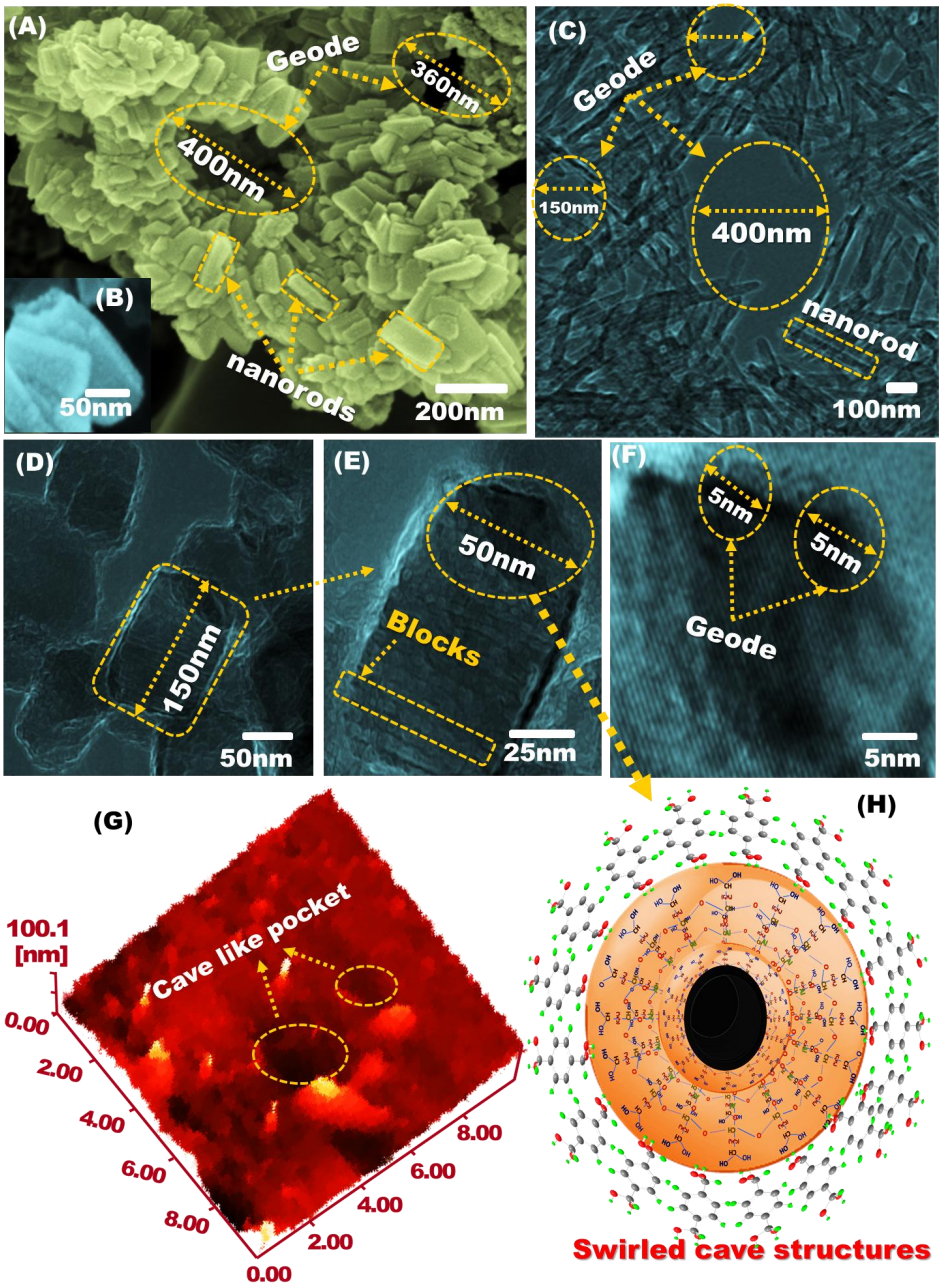

Figure 1. FE-SEM images (A) of aluminum organic-inorganic nanorods with geodes shells morphology b) High-magnification FE-SEM images of nanorods with geodes shells. Low- and

high-magnification STEM (C-F) of hierarchal geodes. G) AFM micrograph of high-order nanorods with geodes shells multiple vast-mouth caves and controllable entrance sizes as vesicle traps. H) the molecular building of crystal structure the tower-like structure of aluminum organic-inorganic frameworks carriers via binding interaction of aluminum salt with terephthalic acid.

A N_2 adsorption–desorption isotherm was used to investigate the surface morphology of the carrier before and after decoration. The measurements confirmed the microporous cage of the carrier and BMAs (Figure S3A). The isotherms of the carrier and BMAs exhibited an unveiled type (I) of adsorption behavior. However, considering the dense decoration of organic colorant L1 on the carrier channels, the N_2 isotherm supported the uniform pore openings (< 2 nm) and microporous cavity (~1.8 nm). The results showed a reduction in the carrier surface area. The surface area of BMAs (683 m^2/g) was less than that of the Al inorganic–organic framework carrier. Moreover, the volume of BMAs pore (0.0964 cm^3/g) was less than that of Al inorganic–organic frameworks (0.16 cm^3/g). Therefore, the remarkable reductions in carrier pore volume and surface area confirmed that the organic colorant receptors successfully shielded the organic–inorganic framework carrier surfaces. The NLDFT/GCMC data were used to examine the scaffold pore type [32]. Figure S3B displays an exceptional peak located at ~1.7 nm, confirming the supermicropore diameters of the inorganic–organic framework carriers and the BMA geodes were distributed within this range. The results revealed the uniform decoration of organic receptor L1 into the microporous cavities of the carriers.

The crystal structure and stability of the supermicroporous carriers and BMAs geodes was confirmed by X-ray diffraction patterns. The results showed well-defined diffraction peaks, revealing the well-organized structure assembly of the carrier and BMA geodes. The highly

ordered peaks situated at 2θ values of 8.1° and 9.1° which matched with the Al inorganic–organic frameworks.[51] These results proved the successful construction of the microporous Al organic–inorganic framework carriers. Furthermore, the retention in Bragg peaks confirmed the colorant j-aggregate receptors of L1 decoration and accumulation into the supermicroporous cavities of the carriers with high crystal-structure stability (Figures S3C and S3D).

The molecular arrangement of the colorant aggregate (L1) in the inorganic–organic architectures were confirmed using optical images (Scheme 3), which showed a branching dendrite molecular aggregation. This optical microscopic observation demonstrated that the spatial orientation of L1 transitioned from H-aggregates in the ethanol solution to form j-aggregates in the solid phase within the trapping of L1 into the surface of the geode-shelled nanorods of the organic–inorganic framework carrier. The BMAs sustaining the dendritic arrangement of colorant aggregates into the carrier surface minimized the formation of H-aggregates as a result of trapping of the j-aggregates' molecular dimensionality. The j-aggregates may form a highly ordered molecular alignment at the exterior surface of the colorant-wrapping architecture nanorods for rapid monitoring of toxic cyanide compounds.

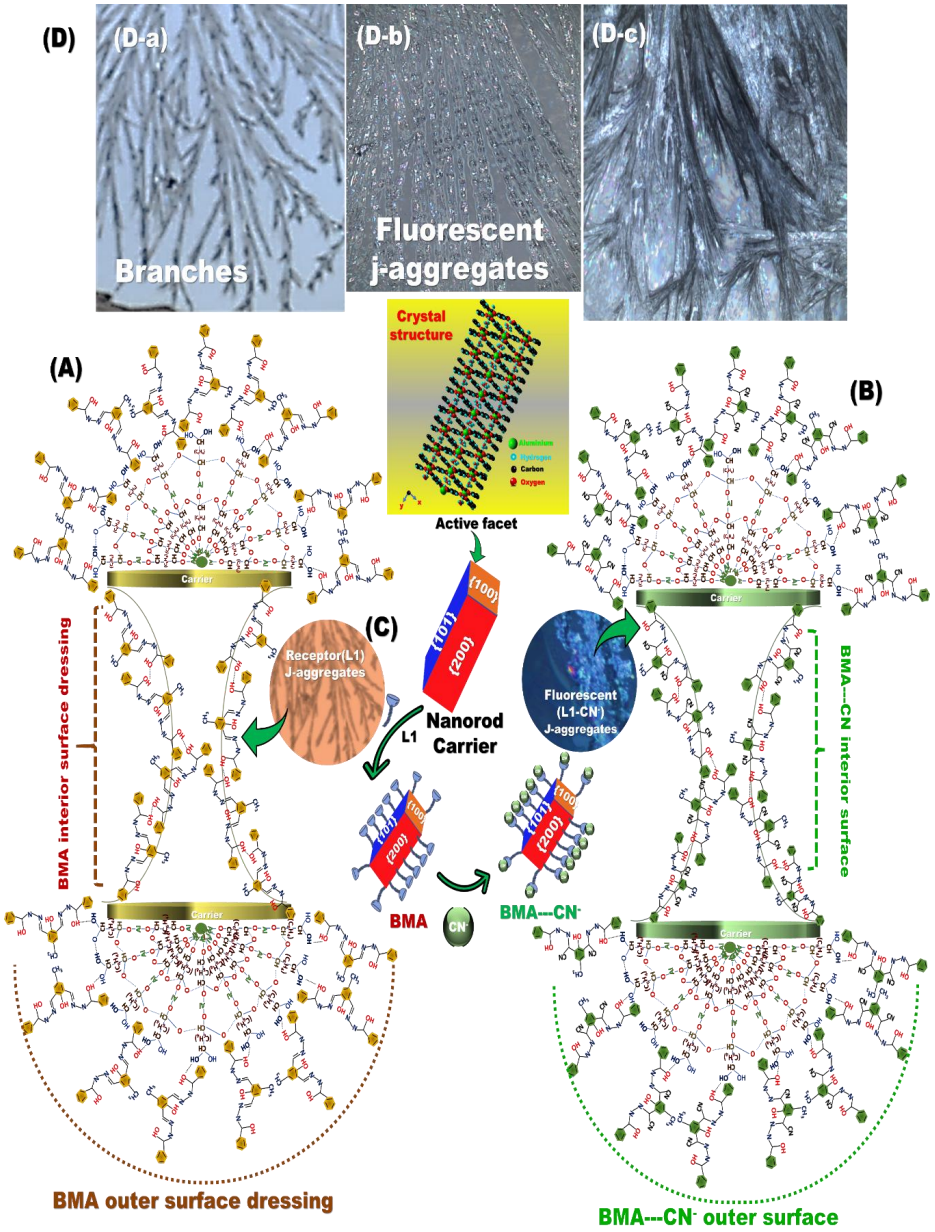

Scheme 3. (A, B) building of molecular structures of colorant and fluorescent j-aggerates of L1 receptor and its [L1-CN] complex into the nanorods with geodes shells surface of inorganic-organic design in the formation BMA and BMA-CN^- design respectively. (C) Schematic design of the interaction and binding of CN^- ion onto nanorods with geodes shells multi-facets interaction surfaces during CN^- ion sensing at pH=3 and recovery of cyanide toxic compounds in living cells and water. (D) The optical microscopic images of the colorant (D-a) and fluorescent

(D-b& D-C) J-aggregates of L1 receptor and its complex with dendritic t (end-to-end) stacking arrangement.

3.3. Exclusive Colorant Tracking of CN^- Ions in Water

The absorption and fluorescence spectra of the organic receptors of L1 were obtained to assess the suitability of the fabricated colorant receptor of L1 for monitoring CN^- ions in homogenous liquid assays. L1 was titrated with CN^- at pH 8.0. The enhancement in absorption intensity of the organic probe L1 was observed at 454 nm, and then it decreased at 363 nm. The isosbestic point at 392 nm was then obtained (Figure 2A). Scheme S1 shows that the yellowish-green color of the organic probe L1 was produced as the CN^- ion concentration gradually increased in the range of 0–2000 parts per billion (ppb). In the fluorometric titration profiles (Figure 2B), the fluorescence intensity at λ_{em} = 540 nm (λ_{ex} = 440 nm) of L1 (20 μM) was augmented upon the successive addition of CN^- ions in ethanol at pH 8.0 (phosphate buffer). The findings showed that the fluorescence intensity was enhanced as the CN^- ion concentration increased and thus confirmed the sensing ability of the colorant aggregates of L1 for CN^- ions via naked-eye inspection under visible light or UV (365 nm, Scheme S1). Under optimal sensing conditions, the absorption and emission spectra were obtained to show the high selectivity of the organic probe L1 to CN^- ions in the presence of various interfering ions, such as F^-, Br^-, Cl^-, I^-, NO_3^-, CH_3COO^-, $H_2PO_4^-$, SO_4^{2-}, ClO_4^-, and HSO_4^-. The results revealed the high stability of the L1–CN^- complex in the presence of common interfering anions. The colorant j-aggregate receptors of L1 discriminated between CN^- and chemically close ions (Figures 2C and 2D).

Under optimal workability conditions, fluorometric titrations were carried out to assess the sensitivity of organic receptors in monitoring CN^- ions (Figures 2F). The linear calibration

curves between the relative colorant j-aggregate receptors of L1 fluorescence intensity of the CN^- ion concentration (ppm) were observed, with a high correlation coefficient ($R^2 = 0.998$).

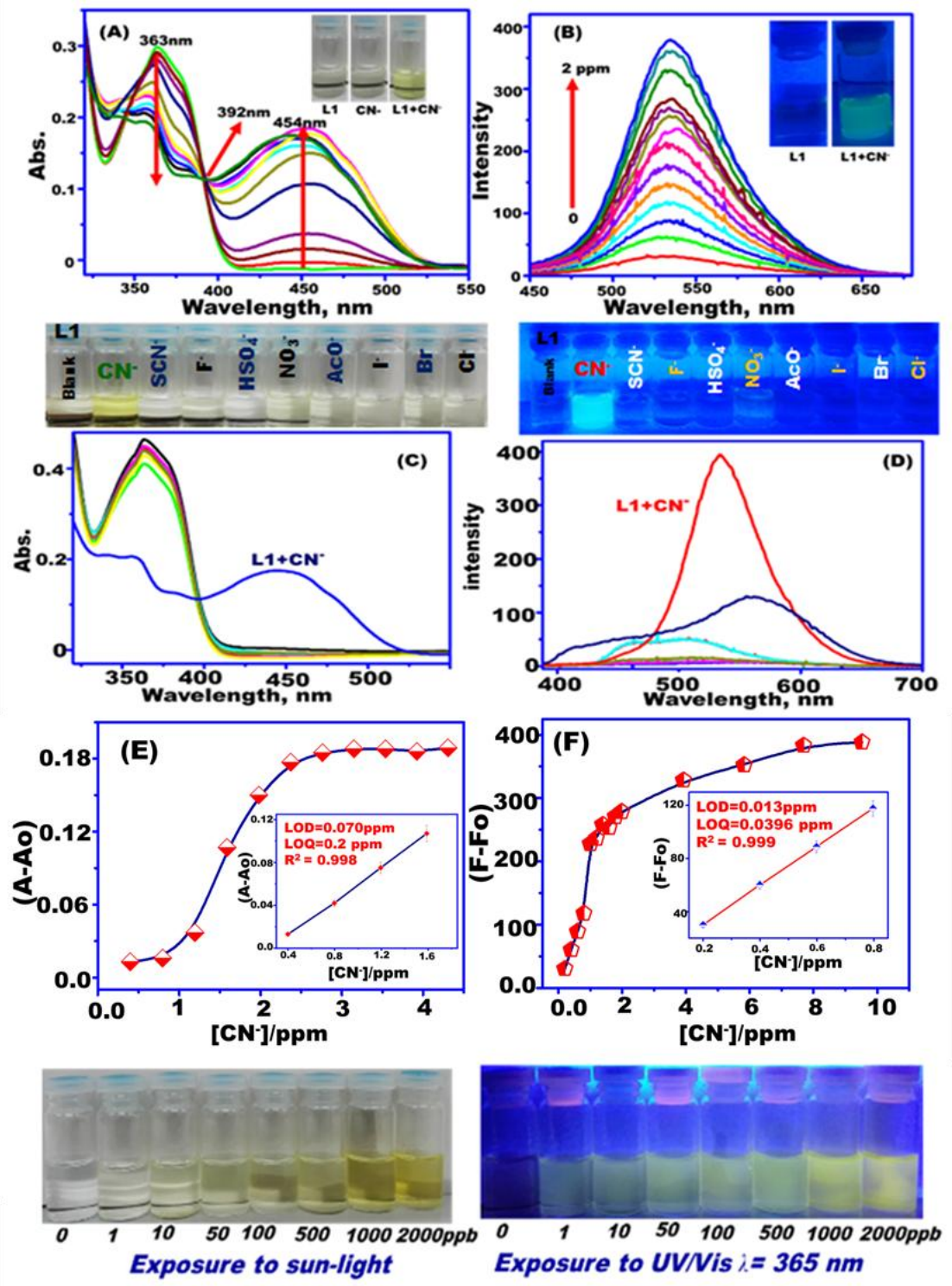

Figure 2. (A) Changes in the UV-vis absorption spectra and (B) fluorescence spectra of L1 solutions in ethanol upon titration with standardized CN^- ions under optimal sensing conditions (pH of 8, staying time of 3 min, the volume of 20 mL, and temperature of 25 °C). Effect of anions as interfering ions on the colorimetric (C) fluorescence spectra (D) of L1. Calibration plots for L1 with absorbance (E) and fluorescence spectra (F) measured for the CN^- ions at λ_{460}, λ_{540} respectively, linear-fit line are inserted in the linear concentration range before the saturation of the calibration plots for the colorimetric and fluorescence spectra of L1 measured at λ_{460}, λ_{540} respectively with different [CN^-] concentrations.

3.4. BMA Detection of CN^- Ions

The sensor amount, contact time or response time, and reaction pH for CN^- ions were investigated to assess the fluorometric sensing assay parameters of BMAs in water. The homogeneity of the BMAs and the ability to detect CN^- ions were then observed using fluorometric sensing assay. The selectivity of the BMAs for CN^- ions was estimated in a mixture of common interfering and multiple anions. With λex = 400 nm, no significant change was observed in the fluorescence intensity of the BMAs. However, a considerable change was found in the emission intensity and color of the BMAs under a UV lamp at 365 nm after adding CN^- ions. This observation confirmed the high sensitivity and selectivity of the BMAs for monitoring ultra-trace concentrations of CN^- ions (Figure 3).

In the fluorescence sensing assays of CN^- ions (Figure 3), a significant enhancement in fluorescence intensity was observed at λem = 460 nm with increasing CN^- ion concentration. Furthermore, the linear calibration curves allowed for detecting CN^- ions with high sensitivity at optimal conditions. Scheme S2 demonstrates the charge transfer mechanism that occurred in the

CN^-–L1 complex at pH 3.0. The remarkable improvement in the sensitivity and selectivity for CN^- ions through the use of BMAs was investigated, as shown in Table 1. Meanwhile, Table 2 shows that the calculated LOD for monitoring CN^- targets by using single BMA geode was up to 88 ppt, which is lower than that in recently reported approaches.

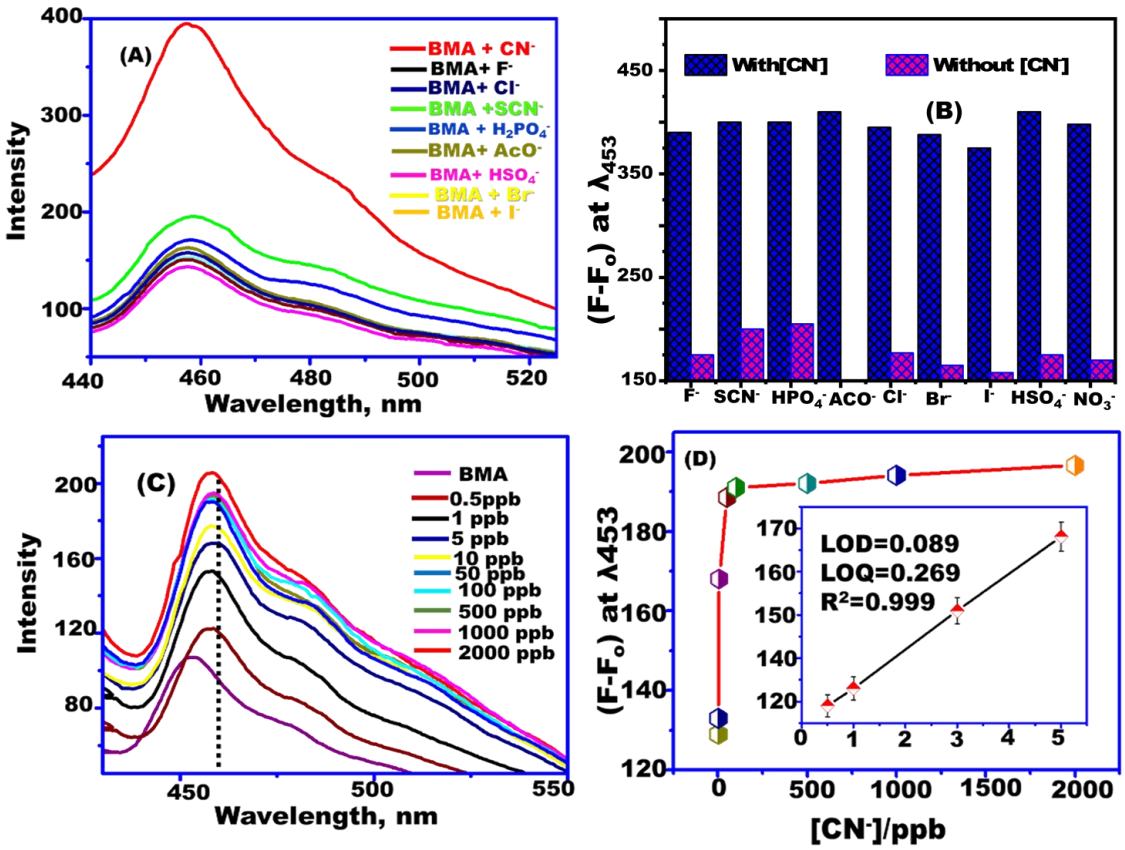

Figure 3. A) Fluorometric spectra of the BMA during the addition of various interfering anions under optimal sensing conditions (pH of 3, staying time of 5 min, BMA amount of 5 mg, volume of 20 mL, and temperature of 25 °C). B) Effect of common interfering anions on fluorescence spectra of BMA in the absence and presence of CN^- ions (2 ppm) under optimal sensing conditions (pH of 3, staying time of 5 min, BMA amount of 5 mg, volume of 20 mL, and temperature of 25 °C). fluorescence spectra (C) and calibration plots (D) of the BMA for the CN^- ions at λ_{453}. A linear-fit line is inserted in the linear concentration range before the saturation of the calibration plots for fluorescence spectra of BMA measured at λ_{453} with different [CN^-]

concentrations under optimal sensing conditions (pH of 3, staying time of 5 min, RFC amount of 5 mg, volume of 20 mL and temperature of 25 °C).

Table 1: Fluorometric sensing of CN^- ions parameters for the organic probe (L1) and BMA.

Parameter	Fluorescent probe (S1)	BMA
Solvent	Ethanol	Milli-Q water
Excitation wavelength	440 nm	400 nm
Emission wavelength	540 nm	453 nm
LOD	13 ppb	0.088 ppb
LOQ	40 ppb	0.2 ppb
Linear rang	2 ppb- 2000ppb	0.5 ppb – 10 ppb
Residual square	0.999	0.999
Specific pH	8	3
Time of response (seconds)	20	15

Table 2: Comparison between the prepared BMA and the reported methods in sensitivity of CN^- ions.

Optical Sensors	Detection limit (ppb)	Ref
HAPQA	15	[64]
IR 786 perchlorate	13	[65]
(Z)-1-((benzo[d]thiazol-ylimino)methyl)naphthalen-2-ol	1560	[66]

imidazo-anthraquinones	93.6	[67]
pyrazine-derived chemosensor	496	[68]
BMA	0.088	Present work

293

294 **3.5. Exclusive Colorant Tracking of CN^- Ions in Biological Cells**

295 Continuous monitoring and visualization of toxic cyanide compounds are important in reducing
296 the health threats associated with toxicant exposure in human cells, particularly in developing
297 countries. Therefore, novel approaches for the detection and colorant tracking of CN^- in
298 contaminated biological cells are imperatively needed. By using MTT protocols, the cell viability
299 and cytotoxicity of the colorant probe L1 and BMAs were investigated in this study. The cells
300 were incubated with different colorant aggregates of L1 and BMA concentrations for 24 h at
301 37 °C. The metabolic activity of the HeLa cells decreased with increasing cytotoxicity of the
302 organic receptors of L1 and the BMA concentration (Figure 4B). The untreated HeLa cells
303 served as the control for all measurements. The colorant aggregates of L1 and BMAs exhibited
304 low cytotoxicity to HeLa cells. For example, 24% of the cells were damaged at a high BMA
305 concentration (50 μg/ml), and 4% of the cells were lost at 10 μg/ml. This result revealed that the
306 cytotoxicity of the organic probe L1 and BMAs did not significantly affect the cell population
307 and led to a low cytotoxicity and cell viability, confirming that the BMAs can be applied for
308 monitoring/tracking/inhibition of CN^- ions in biological cells.

309 **3.6. Visualization of CN^- ions in HeLa cells**

310 Confocal fluorescence microscopy was performed to investigate the monitoring and colorant
311 tracking of CN^- ions in HeLa cells. Such capability can be attributed to the high biocompatibility
312 of the BMAs. First, the HeLa cells were incubated with BMAs (20.0 μg/ml) in PBS buffer for 30

313 min at 37 °C and visualized using confocal fluorescence microscopy with an excitation
314 wavelength of 488 nm (Figure 4A). The results revealed that the cells incubated with BMAs
315 displayed very weak fluorescence. Moreover, the high biocompatibility and low toxicity were
316 investigated via confocal microscopic visualization of cells incubated with the BMAs (20.0
317 μg/ml) and the control. No shrinkage nor damage was visualized on the cell membrane, and the
318 microunit of the BMAs was clearly obtained by cell imaging. The extracellular medium of the
319 HeLa cells was washed off with buffer several times to remove excessive BMAs. The BMA-
320 treated cells were supplemented with 100 ppb CN^- in a medium with polyethersulphone buffer
321 for 30 min at 37 °C. The results showed that the intracellular area fluorescence intensity was
322 enhanced. Throughout the imaging experiments, the HeLa cells were viable, as demonstrated by
323 the bright-field transmission images and confocal microscopic images of the HeLa cells treated
324 with BMA geodes and CN^- ions (Scheme 1). Thus, BMAs can be applied as biocompatible
325 fluorescent nanomonitors for visualizing/tracking CN^- ions in living cells (Figure 4C).

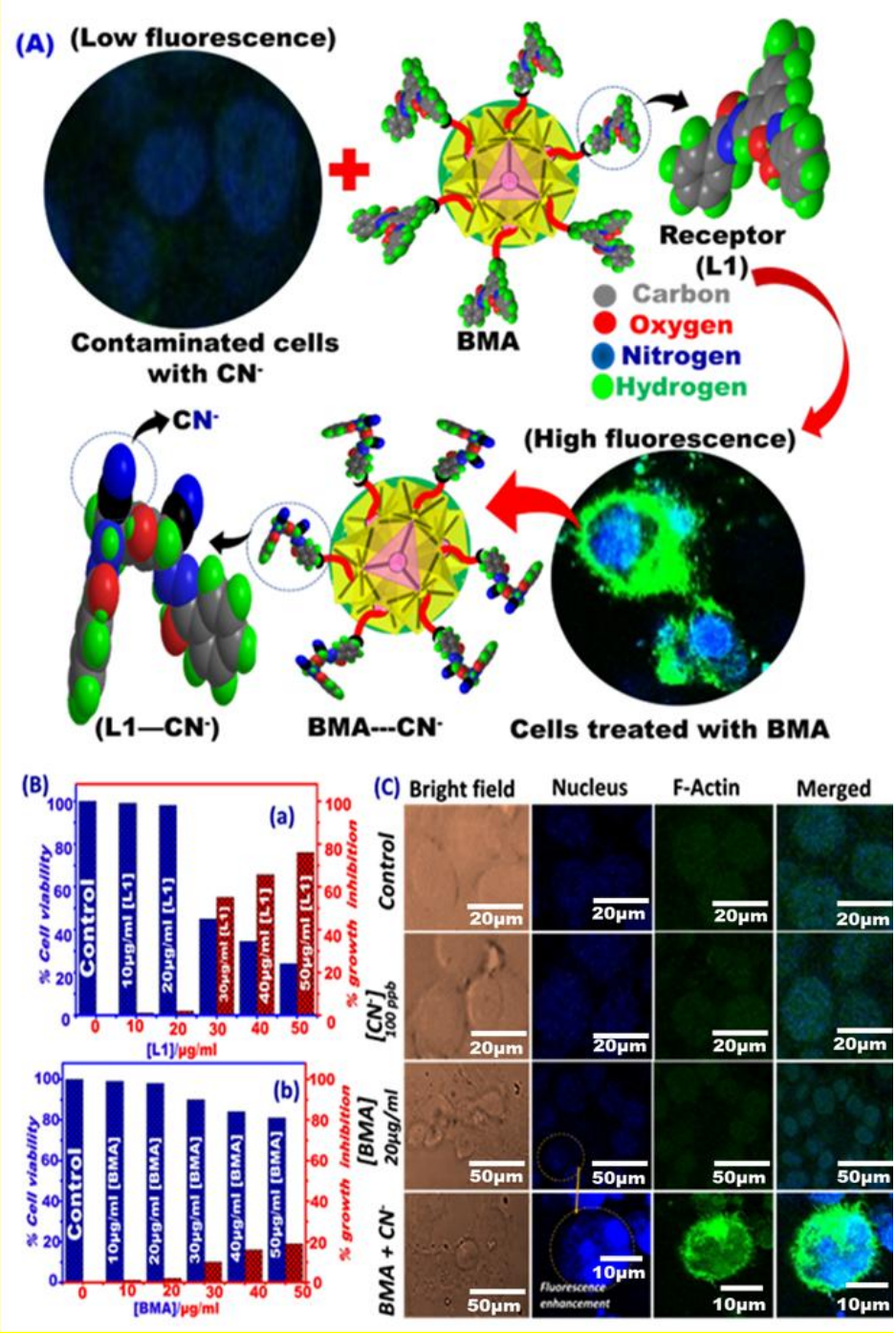

Figure 4. A) Schematic representation illustrates the fluorescence enhancement after the binding interaction between CN^- ions and the biocompatible (BMA) in HeLa cells. B) Percentage (%) of cell viability and (%) of cell inhibition of HeLa cells treated with different concentrations (10-50 μg/ml) of L1 (a), (10-50 μg/ml) of BMA (B). C) Confocal microscope images recorded at excitation wavelength of 488 nm and emission wavelength at 540 nm of control and HeLa cells

with incubated 10 μg/mL BMA with 10μM CN^- for 30 min and HeLa cells with incubated 10 μM of organic probe L1 with 10μM [CN^-] for 30 min.

3.7. Fluorescence-activated Cell Sorting

The cellular volume in flow cytometry was estimated via forward scattering (FSC) intensity, which was obtained for the HeLa cells treated with BMAs. The findings for the BMAs with CN^- ions were close to those for the control cells. Figure 5 shows that the FSC intensity was nearly constant. The change in FSC intensity may be ascribed to the swelling or shrinking of cells as a result of the cell death process. The flow cytometry results revealed that the monitoring of CN^- ions in living cells were not due to the total cell death. Overall, the data confirmed the high biocompatibility features of BMAs under optimal conditions, matching the results obtained from the cytotoxicity studies. The majority of the untreated control cells were viable (99.14%). By contrast, 3.04% of the pierced cells with BMAs were fluorescein isothiocyanate (FITC)-positive apoptotic cells. The data demonstrated that the BMAs did not drastically enhance the percentage of FITC-positive apoptotic cells in comparison with the untreated cells (Figure 5). The low BMA concentration allowed for the improved monitoring of CN^- ions at optimal cellular conditions.

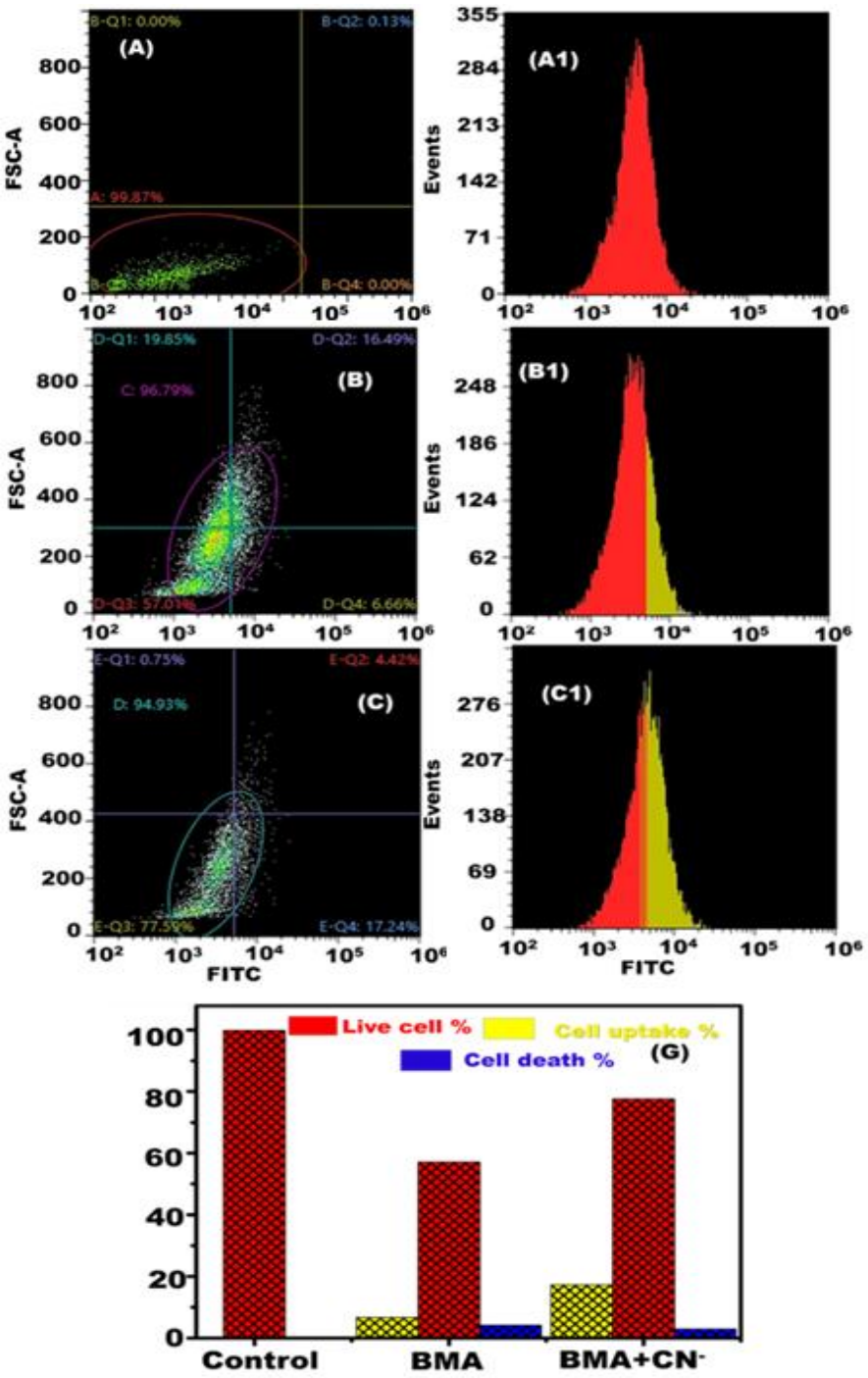

Figure 5. The flow cytometry of the examined BMA geodes in presence and in absence of CN^- ions. HeLa cells were incubated for 24h without any material act as a control (A, A1) followed by incubation for 4 hours with 20 µg/mL [BMA] (B, B1) and with 20 µg/mL [BMA] +100 ppb of [CN^-] (C, C1). (D) statistical results of the examined BMA in presence and in absence of CN^-.

3.8. Tracking/Monitoring of CN^- Ions in HeLa Cells

The HeLa cell concentration in a 96-well black dish was adjusted to quantify CN^- ions and detect them in HeLa cells. The concentration of BMAs was adjusted, with no remarkable effect on the HeLa cells. The untreated HeLa cells initially incubated for 24 h served as the control. The fluorescence enhancement depended on the concentration of the CN^- ions. Figure 6A shows that time did not remarkably affect the recorded fluorescence intensity of CN^- ion monitoring. The emission intensity enhanced with increasing CN^- levels (Figure 6B). The enhanced emission intensity was then recorded using a spectrofluorometer and a microplate reader.

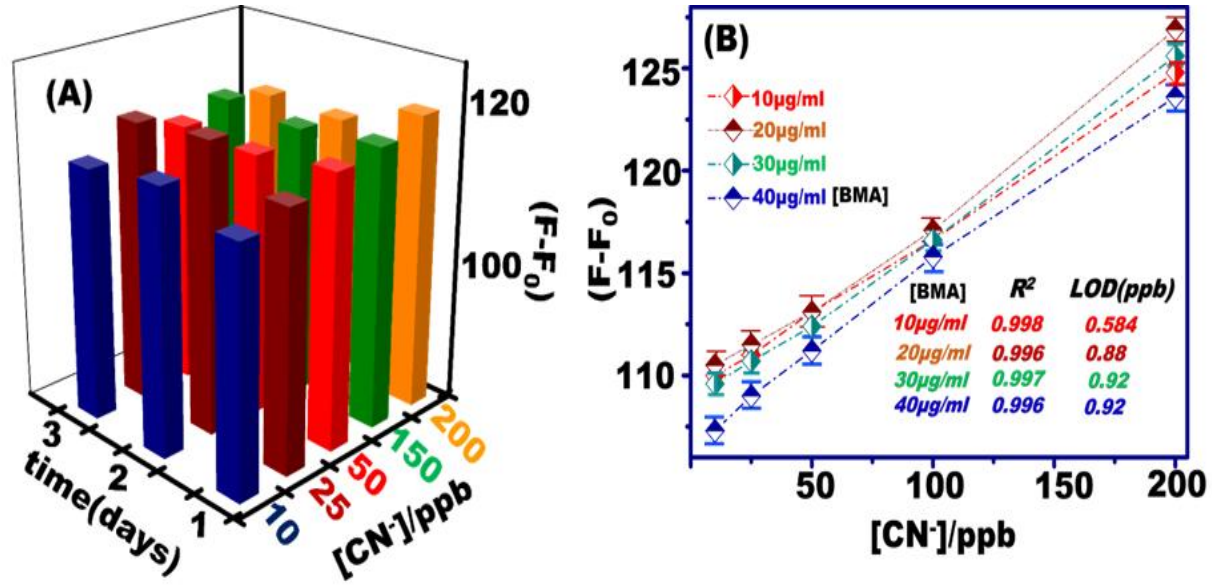

Figure 6. A) Time dependent fluorescence enhancement of living cell line stimulated by 20 µg/ml [BMA] with different concentration of CN^- ions. B) Calibration curve of 10, 20, 30, 40 µg/ml [BMA] against different concentration of CN^- that were induced in PBS solution at pH=7.4.

4. CONCLUSIONS

Contaminated cyanide compounds in the ecosystem are a critical concern owing to the growing of urbanization. The significant health problems caused by toxic cyanide compounds are of interest because of their immutability in the ecosystem. Therefore, ultrasensitive approaches for detection/recovery of CN^- ions in HeLa Cells are urgently needed. BMA geodes were successfully fabricated for tracking and monitoring of toxic CN^- ion concentrations in HeLa cells within few seconds. The BMAs were decorated via direct dressing approaches by wrapping the hydrophobic colorant L1 onto the geode-shelled nanorods of porous organic–inorganic Al frameworks. The BMA geodes exhibited high biocompatibility and cell viability through CN^- ion detection and monitoring in biological trials. Moreover, the fluorescence intensity of the intracellular area enhanced after CN^- ions were added. Under specific conditions, the results confirmed the high applicability of BMA geodes for in-vitro fluorescence of CN^- ion tracking/sensing in HeLa cells, indicating the BMA geode-shelled nanorods' capability in reducing health hazards due to toxicant exposure.

REFERENCES

[1] S. Malkondu, S. Erdemir, S. Karakurt, Red and blue emitting fluorescent probe for cyanide and hypochlorite ions: Biological sensing and environmental analysis. Dyes and Pigments, 174 (2020)108019.

[2] T.B. Hendry-Hofer, P.C. Ng, A.E. Witeof, S.B. Mahon, M. Brenner, G.R. Boss, V.S. Bebarta, A review on ingested cyanide: risks, clinical presentation, diagnostics, and treatment challenges. Journal of Medical Toxicology., 15 (2019) 128-133.

[3] Guidelines for Drinking-water Quality, World Health Organization, Geneva, (1996).

[4] G.D. Muir, Hazards in Chemical Laboratory, The Royal Chemical Society,London, (1977).

[5] S. Erdemir, S. Malkondu, On-site and low-cost detection of cyanide by simple colorimetric and fluorogenic sensors: smartphone and test strip applications. Talanta, 207 (2020) 120278.

[6] M.T. Waseem, H.M. Junaid, S. Majeed, A.M. Khan, T. Mahmood, S.A. Shahzad, Fluorene based fluorescent and colorimetric chemosensors for selective detection of cyanide ions in aqueous medium and application of logic gate. Microchemical Journal, 173 (2022) 107018.

[7] E. Kandemir, M. Özkütük, B. Aydıner, N. Seferoğlu, H. Erer, Z. Seferoğlu, Novel fluorescent coumarin-thiazole based sensors for selective determination of cyanide in aqueous media. Journal of Molecular Structure, 1249 (2022) 131593.

[8] S.K. Pramanik, A. Das, Fluorescent probes for imaging bioactive species in subcellular organelles. Chemical Communications, 57(91) (2021) 12058-12073.

[9] L. Chen, C. Fu, Z. Li, T. Zhu, X. Chen, C. Gao, T. Wang, W. Pang, C. Liu, A new strategy for sensing cyanide ions by cyanide-induced nucleophilic substitution of hydrogen in nitro-controlled electron-deficient fluorophores. Tetrahedron Letters, 61(12) (2020) 151656.

[10] T. Devendhiran, K. Kumarasamy, M.C. Lin, Y.X. Yang, Synthesis and physical studies of coumarin-based chemosensor for cyanide ions. Inorganic Chemistry Communications, 134 (2021) 108951.

[11] E. Keleş, B. Aydıner, Y. Nural, N. Seferoğlu, E. Şahin, Z. Seferoğlu, A new mechanism for selective recognition of cyanide in organic and aqueous solution. European Journal of Organic Chemistry, 2020(30) (2020) 4681-4692.

[12] Y. Nural, E. Karasu, E. Keleş, B. Aydıner, N. Seferoğlu, Ç. Efeoğlu, E. Şahin, Z. Seferoğlu, Synthesis of novel acylthioureas bearing naphthoquinone moiety as dual sensor for high-

performance naked-eye colorimetric and fluorescence detection of CN− and F− ions and its application in water and food samples. Dyes and Pigments, 198 (2022) 110006.

[13] T. Peng, S. Li, Y. Zhou, R. Liu, J. Qu, Two cyanoethylene-based fluorescence probes for highly efficient cyanide detection and practical applications in drinking water and living cells. Talanta, 234 (2021) 122615.

[14] M. Qiao, R. Zhang, S. Liu, J. Liu, L. Ding, Y. Fang, Imidazolium-Modified Bispyrene-Based Fluorescent Aggregates for Discrimination of Multiple Anions in Aqueous Solution. *ACS Applied Materials & Interfaces*, *14*(28) (2022) 32706-32718.

[15] C. Nandhini, P.S. Kumar, K. Poongodi, R. Shanmugapriya, K.P. Elango, Development of simple imine-based probe for selective fluorescent cyanide sensing with red-emission in solid and solution phases. Journal of Molecular Liquids, 327 (2021) 114833.

[16] A. Tigreros, J.C. Castillo, J. Portilla, Cyanide chemosensors based on 3-dicyanovinylpyrazolo [1, 5-a] pyrimidines: effects of peripheral 4-anisyl group substitution on the photophysical properties. Talanta, 215 (2020) 120905.

[17] I.M. El-Sewify, M.M. Khalil, Mesoporous nanosensors for sensitive monitoring and removal of copper ions in wastewater samples. New Journal of Chemistry, 45(5) (2021) 2573-2581.

[18] S.A. El-Safty, M.A. Shenashen, Optical mesosensor for capturing of Fe (III) and Hg (II) ions from water and physiological fluids. Sensors and Actuators B: Chemical 183 (2013)70.

[19] S.A. El-Safty, M. Khairy, M.A. Shenashen, E. Elshehy, W. Warkocki, M. Sakai, Optical Mesoscopic Membrane Sensor Layouts for Water-Free and Blood-Free Toxicants, *Nano Res*, 8*(10*) (2015) 3150–3163.

[20] S. A. El-Safty, M. Sakai, M. M. Selim, A. A. Hendi, Mesosponge Optical Sinks for Multifunctional Mercury Ion Assessment and Recovery from Water Sources, *ACS Appl. Mater. Interfaces, 7 (24)* (2015) 13217-13231.

[21] W. Warkocki, S.A. El-Safty, M.A. Shenashen, E. Elshehy,Yamaguchi, H. Photo-Induced Recovery, Optical Detection, and Separation of Noxious Seo_3^{2-} Using A Mesoporous Nanotube Hybrid Membrane, *J. Mater Chem. A*, *3 (34)* (2015) 17578-17589.

[22] W. Li, C. Jiang, S. Lu, F. Wang, Z. Zhang, T. Wei, Y. Chen, J. Qiang, Z. Yu, X. Chen, A hydrogel microsphere-based sensor for dual and highly selective detection of Al^{3+} and Hg^{2+}. Sensors and Actuators B: Chemical, 321 (2020) 128490.

[23] H. G. Gomaa, H. Khalifa, M. Selim, M. A. Shenashen, S. Kawada, A. S. Alamoudi, A. Azzam, A.A. Alhamid, S. A. El-Safty, Selective, Photoenhanced Trapping/Detrapping of Arsenate Anions Using Mesoporous Blobfish Head TiO_2 Monoliths, *ACS Sustain. Chem. Eng. 5 (11)* (2017)10826–10839.

[24] S.A. El-Safty, M. Sakai, M. M. Selim, A.A. Alhamide, *One*-Pot Layer Casting-Guided Synthesis of Nanospherical Aluminosilica@Organosilica@Alumina Core–Shells Wrapping Colorant Dendrites for Environmental Application, *RSC Advances***.** *5 (74)* (2015)60307-60321.

[25] M. A. Shenashen, S. A. El‐Safty, E.A. Elshehy, M. Khairy, Selective Recovery of Silver(I) Ions from E-Waste using Cubically Multithiolated Cage Mesoporous Monoliths, *Eur. J. Inorg. Chem*. 2015*(1)* (2015) 179-191.

[26] E. A. Elshehy, S.A. El-Safty, M.A. Shenashen, M. Khairy. Design and Evaluation of Optical Mesocaptor for The Detection/Recovery of Au(III) From an Urban Mine, *Sens. Actua B: Chem. 203* (2014) 363-374.

[27] H. Gomaa, M. A. Shenashen, M.F. Cheira, K. Sueki, T.A. Seaf El-Nasr, M.M. Selim, S.A. El-Safty, "A novel, spongy mesoporous hybrid bio-adsorbents derived from agricultural waste for highly selective thorium recovery", Journal of Cleaner Production, 402 (2023) 136819.

[28] H. Gomaa, M. A. Shenashen, A. Elbaz, S. Kawada, T.A. Seaf El-Nasr, M.F. Cheira, A.I. Eid, S.A. El-Safty, Inorganic-organic mesoporous hybrid segregators for selective and sensitive extraction of precious elements from urban mining, Journal of Colloid and Interface Science 604 (2021) 61-79.

[29] G. Sivaraman, M. Iniya, T. Anand, N.G. Kotla, O. Sunnapu, S. Singaravadivel, A. Gulyani, and D. Chellappa, Chemically diverse small molecule fluorescent chemosensors for copper ion. Coordination Chemistry Reviews, 357(2018)50-104.

[30] P.C.A. Swamy, G. Sivaraman, R.N. Priyanka, S.O. Raja, K. Ponnuvel, J. Shanmugpriya, A. Gulyani, Near Infrared (NIR) absorbing dyes as promising photosensitizer for photo dynamic therapy. Coordination Chemistry Reviews, 411(2020)213233.

[31] G. Sivaraman, B. Vidya, D. Chellappa,. Rhodamine based selective turn-on sensing of picric acid. RSC Advances, 4(58) (2014)30828-30831.

[32] G.G.V. Kumar, M.P. Kesavan, G. Sivaraman, J. Rajesh, Colorimetric and NIR fluorescence receptors for F− ion detection in aqueous condition and its Live cell imaging. Sensors and Actuators B: Chemical, 255(2018)3194-3206.

[33] B. Vidya, M. Iniya, G. Sivaraman, R.V. Sumesh, Diverse benzothiazole based chemodosimeters for the detection of cyanide in aqueous media and in HeLa cells. Sensors and Actuators B: Chemical, 242(2017)434-442.

[34] E. Ramachandran, S.A. Vandarkuzhali, G. Sivaraman, R. Dhamodharan, Phenothiazine Based Donor–Acceptor Compounds with Solid-State Emission in the Yellow to NIR Region and Their Highly Selective and Sensitive Detection of Cyanide Ion in ppb Level. Chemistry–A European Journal, 24(43)(2018)11042-11050.

[35] S.O. Raja, G. Sivaraman, S. Biswas, G. Singh, F. Kalim, P. Kandaswamy, A. Gulyani,. A tunable palette of molecular rotors allows multicolor, ratiometric fluorescence imaging and direct mapping of mitochondrial heterogeneity. ACS Applied Bio Materials, 4(5)(2021)4361-4372.

[36] S. Perumal, S. Karuppannan, S. Gandhi, S. Subramanian, A. Govindasamy, S.K. Gopal,. Bithiophene triarylborane dyad: An efficient material for the selective detection of CN− and F− ions. Applied Organometallic Chemistry, 34(1) (2020)e5257.

[37] S. Gouthaman, A. Jayaraj, M. Sugunalakshmi, G. Sivaraman,. Supramolecular self-assembly mediated aggregation-induced emission of fluorene-derived cyanostilbenes: multifunctional probes for live cell-imaging. Journal of Materials Chemistry B, 10(13)(2022)2238-2250.

[38] G. Mahalakshmi, P.S. Kumar, G. Sivaraman, M.S. Perumal, K.P. Elango, A simple imine as a dual-channel chemosensor for detection of CN− and HS− ions via different mechanisms in organic and aquo-organic media. Journal of Photochemistry and Photobiology A: Chemistry, 406(2021)113021.

[39] P. Chandrasekaran, G. Sivaraman, S. Rasala, M.G. Sethuraman, N.G. Kotla, Y. Rochev, Quercetin conjugated fluorescent nitrogen-doped carbon dots for targeted cancer therapy application. Soft Matter, 18(30)(2022)5645-5653.

503 [40] H. Gomaa, M. A. Shenashen, A. Elbaz, H. Yamaguchi, M. Abdelmottaleb, S.A. El-Safty,
504 Mesoscopic engineering materials for visual detection and selective removal of copper ions
505 from drinking and wastewater sources, Journal of Hazardous Materials 406 (2021) 124314.
506 [41] M.Y. Emran, M. A. Shenashen, A.I. Eid, M.M. Selim, S.A. El-Safty, Portable sensitive
507 and selective biosensing assay of dopamine in live cells using dual phosphorus and nitrogen
508 doped carbon urchin-like structure, Chemical Engineering Journal, 430 (4) (2022) 132818.
509 [42] [31] M.Y. Emran, M. A. Shenashen, A. Elmarakbi, M.M. Selim, S.A. El-Safty, Nitrogen-
510 doped carbon hollow trunk-like structure as a portable electrochemical sensor for
511 noradrenaline detection in neuronal cells, Analytica Chimica Acta, 1192 (2022) 339380.
512 [43] M.Y. Emran, S.A. El-Safty, A. Elmarakbi, A. Reda, A. EL Sabagh, M. A. Shenashen,
513 Chipset Nanosensor Based on N‐Doped Carbon Nanobuds for Selective Screening of
514 Epinephrine in Human Samples, Advanced Materials Interfaces, 9(1) (2022) 2101473.
515 [44] W.J. Perry, A. Weiss, R. Van de Plas, J.M. Spraggins, R.M. Caprioli, E.P. Skaar,
516 Integrated molecular imaging technologies for investigation of metals in biological systems:
517 A brief review. Current opinion in chemical biology, 55 (2020) 127-135.
518 [45] S. Mandal, S. Natarajan, P. Mani, A. Pankajakshan, Post‐synthetic modification of
519 metal–organic frameworks toward applications. Advanced Functional Materials, 31(4) (2021)
520 (2021) 2006291.
521 [46] Y.S. Kang, Y. Lu, K. Chen, Y. Zhao, P. Wang, W.Y. Sun, Metal–organic frameworks
522 with catalytic centers: From synthesis to catalytic application. Coordination chemistry
523 reviews, 378 (2019) 262-280.
524 [47] R. Haldar, S. Bhattacharyya, T.K. Maji, Luminescent metal–organic frameworks and
525 their potential applications. Journal of Chemical Sciences, 132 (2020) 1-25.

526 [48] L. Shao, X. Hu, K. Sikligar, G.A. Baker, J.L. Atwood, Coordination Polymers
527 Constructed from Pyrogallol [4] arene-Assembled Metal–Organic Nanocapsules. Accounts
528 of Chemical Research, 54(16) (2021) 3191-3203.
529 [49] Y.H. Zou, Y.B. Huang, D.H. Si, Q. Yin, Q.J. Wu, Z. Weng, R. Cao, Porous metal–
530 organic framework liquids for enhanced CO2 adsorption and catalytic conversion.
531 Angewandte Chemie, 133(38) (2021) 21083-21088.
532 [50] M.A. Little, A.I. Cooper, The chemistry of porous organic molecular materials.
533 Advanced Functional Materials, 30(41) (2020) 1909842.
534 [51] O.M. Yaghi, Metal–Organic Frameworks: A Tale of Two Entanglements, Nat. Mater. *6*
535 (2007) 92–93.
536 [52] I.M. El-Sewify, M. A. Shenashen, A. Shahat, H. Yamaguchi, M.M. Selim, M.M.H.
537 Khalil, S.A. El-Safty, "Ratiometric Fluorescent Chemosensor Zn^{2+} Ions in Environmental
538 Samples using Supermicroporous Organic-Inorganic Structures as Potential Platforms"
539 ChemistrySelect 2 (34) (2017) 11083-11090.
540 [53] S.A. El-Safty, A. Ismail, T. Hanaoka, H. Matsunaga, F. Mizukami, Optical Nanoscale
541 Pool-on-Surface Design for Control Sensing Recognition of Multiple Cations, *Adv. Funct.*
542 *Mater*. *18* (2008) 1485.
543 [54] M.A. Shenashen, S. A. El-Safty, E. A. Elshehy “Monolithic scaff olds for highly
544 selective ion sensing/removal of Co(II), Cu(II), and Cd(II) ions in water”, Analyst. 139(24)
545 (2014) 6393-6405.
546 [55] a)M.A. Shenashen, S. A. El-Safty, E.A. Elshehy “Architecture of Optical Sensor for
547 Recognition of Multiple Toxic Metal ions from Water” Journal of Hazardous Materials, 260
548 (2013) 833-843; b) M.A. Shenashen, E.A. Elshehy, S. A. El-Safty, M. Khairy “Visual

monitoring and removal of divalent copper, cadmium, andmercury ions from water by using mesoporous cubic Ia3d aluminosilica sensors" Separation and Purification Technology 116, (2013) 73–86.

[56] S.A. El-Safty, M.A. Shenashen, A. Shahat "Tailor-Made Micro-Object Optical Sensor Based on Mesoporous Pellets for Visual Monitoring and Removal of Toxic Metal Ions from Aqueous Media" small 9(13) (2013) 2288-2296.

[57] S. Ehrling, E.M. Reynolds, V. Bon, I. Senkovska, T.E. Gorelik, J.D. Evans, M. Rauche, M. Mendt, M.S. Weiss, A. Pöppl, E. Brunner, Adaptive response of a metal–organic framework through reversible disorder–disorder transitions. Nature Chemistry, 13(6) (2021) 568-574.

[58] M.Y. Emran,M. Mekawy, N. Akhtar, M. A. Shenashen, I.M. El-Sewify. A. Faheem, S.A. El-Safty "Broccoli-shaped biosensor hierarchy for electrochemical screening of noradrenaline in living cells", Biosensors & Bioelectronics 100 (2018) 122-131

[59] M.Y. Emran, H. Khalifa, H. Gomaa, M.A. Shenashen, N. Akhtar, M. Mekawy, A. Faheem, S.A. El-Safty "Hierarchical C-N doped NiO with dual-head echinop flowers for ultrasensitive monitoring of epinephrine in human blood serum", Microchimica Acta, 184 (2017) 4553–4562.

[60] A.M. Azzam, M. A. Shenashen, M.M. Selim, H. Yamaguchi, I.M. ElSewify, S. Kawada, A.A. Alhamid, S.A. El-Safty "Nanospherical inorganic α-Fe core-organic shell necklaces for the removal of arsenic(V) and chromium(VI) from aqueous solution", Journal of Physics and Chemistry of Solids, 109 (2017) 78-88.

[61] N. Akhtar, M.Y. Emran, M. A. Shenashen, H. Khalifa, T. Osaka, A. Faheem, T. Homma, H. Kawarada, S.A. El-Safty, "Fabrication of Photo-electrochemical biosensor for

572 ultrasensitive screening of mono-bioactive molecules: effect of geometrical structures and
573 crystal surfaces", Journal of Materials Chemistry B 5 (2017) 7985-7996.
574 [62] E.S.M. El-Sayed, Y.D. Yuan, D. Zhao, D. Yuan, Zirconium Metal–Organic Cages:
575 Synthesis and Applications. Accounts of Chemical Research, 55(11) (2022) 1546-1560.
576 [63] S. Basu Roy, A. Maity, K. K. Rajak, A Turn-Off Fluorescence Sensor for Cyanide
577 Detection Which In Turn Inhibit 2-Way ESIPT Investigated By Experimental And
578 Theoretical Study, Inorg. Chem. Commun. 76 (2017) 81–86.
579 [64] B. Barare, I. Babahan, Y. M. Hijji, E. Bonyi, S. Tadesse, K. Aslan, Highly Selective
580 Sensor for Cyanide in Organic Media and on Solid Surfaces, *Sensors*. *16* (2016) 271
581 [65] G.R. You, G.J. Park, S.A. Lee, Y.W. Choi, Y.S. Kim, J.J. Lee, C. Kim, A Single
582 Chemosensor for Multiple Target Anions: The Simultaneous Detection Of CN− And Oac− In
583 Aqueous Media, *Sensor Actuat B*, 202 (2014) 645–655.
584 [66] R.M.F. Batista, S. P.G. Costa, M.M.M. Raposo, Selective Colorimetric and Fluorimetric
585 Detection of Cyanide Inaqueous Solution Using Novel Heterocyclic Imidazo-Anthraquinones,
586 *Sensor Actuat B*. *191* (2014) 791– 799.
587 [67] J.J. Lee, G. J. Park, Y. W. Choi, G. R. You, Y. S. Kim, S. Y. Lee, C. Kim, Detection of
588 Multiple Analytes (CN− and F−) Based on A Simple Pyrazine-Derived Chemosensor in
589 Aqueous Solution: Experimental and Theoretical Approaches, *Sensor Actuat B*. *207* (2015)
590 123–132.
591 [68] Y.J. Na, G.J. Park, H.Y. Jo, S.A. Leea, C. Kim colorimetric chemosensor based on a
592 Schiff base for highly selective sensing of cyanide in aqueous solution: the influence of
593 solvents, *New J. Chem. 38* (2014) 5769.